

## SAR sensing of the atmosphere: stack-based processing for tropospheric and ionospheric phase retrieval

Marco Manzoni, Naomi Petrushevsky, Chuanjun Wu, Stefano Tebaldini, Andrea Virgilio Monti-Guarnieri & Mingsheng Liao

To cite this article: Marco Manzoni, Naomi Petrushevsky, Chuanjun Wu, Stefano Tebaldini, Andrea Virgilio Monti-Guarnieri & Mingsheng Liao (21 Mar 2024): SAR sensing of the atmosphere: stack-based processing for tropospheric and ionospheric phase retrieval, Geo-spatial Information Science, DOI: [10.1080/10095020.2024.2330556](https://doi.org/10.1080/10095020.2024.2330556)

To link to this article: <https://doi.org/10.1080/10095020.2024.2330556>



© 2024 Wuhan University. Published by Informa UK Limited, trading as Taylor & Francis Group.



Published online: 21 Mar 2024.



Submit your article to this journal [↗](#)



Article views: 349









View related articles [↗](#)



View Crossmark data [↗](#)

# SAR sensing of the atmosphere: stack-based processing for tropospheric and ionospheric phase retrieval

Marco Manzoni <sup>a</sup>, Naomi Petrushevsky <sup>a</sup>, Chuanjun Wu <sup>a,b</sup>, Stefano Tebaldini <sup>a</sup>, Andrea Virgilio Monti-Guarnieri <sup>a</sup> and Mingsheng Liao <sup>b</sup>

<sup>a</sup>Department of Electronics, Information, and Bioengineering, Politecnico di Milano, Milano, Italy; <sup>b</sup>State Key Laboratory of Information Engineering in Surveying, Mapping and Remote Sensing, Wuhan University, Wuhan, China

## ABSTRACT

This paper is intended to summarize the research conducted during the first 2 years of the Dragon 5 project 59,332 (geophysical and atmospheric retrieval from Synthetic Aperture Radar (SAR) data stacks over natural scenarios). Monitoring atmospheric phenomena, encompassing both tropospheric and ionospheric conditions, holds pivotal significance for various scientific and practical applications. In this paper, we present an exploration of advanced techniques for estimating tropospheric and ionospheric phase screens using stacks of Synthetic Aperture Radar (SAR) images. Our study delves into the current state-of-the-art in atmospheric monitoring with a focus on spaceborne SAR systems, shedding light on their evolving capabilities. For tropospheric phase screen estimation, we propose a novel approach that jointly estimates the tropospheric component from all the images. We discuss the methodology in detail, highlighting its ability to recover accurate tropospheric maps. Through a series of quantitative case studies using real Sentinel-1 satellite data, we demonstrate the effectiveness of our technique in capturing tropospheric variability over different geographical regions. Concurrently, we delve into the estimation of ionospheric phase screens utilizing SAR image stacks. The intricacies of ionospheric disturbances pose unique challenges, necessitating specialized techniques. We dissect our approach, showcasing its capacity to mitigate ionospheric noise and recover precise phase information. Real data from the Sentinel-1 satellite are employed to showcase the efficacy of our method, unraveling ionospheric perturbations with improved accuracy. The integration of our techniques, though presented separately for clarity, collectively contributes to a comprehensive framework for atmospheric monitoring. Our findings emphasize the potential of SAR-based approaches in advancing our knowledge of atmospheric processes, thus fostering advancements in weather prediction, geophysics, and environmental management.

## ARTICLE HISTORY

Received 1 February 2023  
Accepted 8 March 2024

## KEYWORDS

SAR; atmosphere;  
ionosphere; troposphere

## 1. Introduction

One major advantage of Synthetic Aperture Radar (SAR) is its ability to collect data independently of weather and lighting conditions. This allows for the acquisition of high-resolution images of the Earth's surface and atmosphere on a consistent basis, providing valuable information for a wide range of applications. SAR data can be collected in different wavelengths, including *P*-, *L*-, *C*-, and *X*-band, each of which has its own advantages and limitations (Morishita and Hanssen 2014). *P*- and *L*-band SAR has a longer wavelength, which allows for better penetration through vegetation but usually provides lower spatial resolution compared to *C*-band and *X*-band SAR. *X*-band SAR, on the other hand, has the highest spatial resolution but cannot penetrate through vegetation. Historically, SAR systems were used to acquire quantities related to objects on the ground, being that deformation of buildings (Ferretti, Prati, and Rocca

2000), urbanization (Petrushevsky, Manzoni, and Monti-Guarnieri 2021), Digital Elevation Models (DEM) (Hensley, Rosen, and Gurrola 2000), the above-ground biomass (AGB) of trees in a forest (Soja et al. 2021) or the detection changes due to illegal operations (Manzoni, Monti-Guarnieri, and Molinari 2021).

Recently, the exploitation of SAR images for atmospheric remote sensing started to play a significant role in the scientific community. The electromagnetic (EM) wave travels through the atmosphere, bounces on the target on the ground, and is reflected back to the receiving antenna. The signature of the atmosphere can then be identified from the retrieved response and studied for different applications. Traditionally, the atmospheric contribution can be split into two main components of interest. The lower layer, known as troposphere, holds the majority of the atmosphere's water vapor. Different conditions

**CONTACT** Stefano Tebaldini  stefano.tebaldini@polimi.it

© 2024 Wuhan University. Published by Informa UK Limited, trading as Taylor & Francis Group.

This is an Open Access article distributed under the terms of the Creative Commons Attribution License (<http://creativecommons.org/licenses/by/4.0/>), which permits unrestricted use, distribution, and reproduction in any medium, provided the original work is properly cited. The terms on which this article has been published allow the posting of the Accepted Manuscript in a repository by the author(s) or with their consent.

in pressure, temperature, and humidity modify the refractive index of the medium, providing valuable information about conditions such as turbulence, rain, and clouds (Mateus et al. 2019). The upper part of the atmosphere, known as the ionosphere, has a high concentration of electrons due to the sun's UV radiation (Wright et al. 2003). In the following analysis, we provide a framework to monitor both phenomena from a time-series of C-Band SAR images. Using a stack instead of just a single interferometric couple leads to a high-quality estimate of the atmospheric components without compromising spatial resolution.

Concerning the troposphere, the non-unitary refractive index leads to an equivalent extra distance traveled by the EM wave or, equivalently, an extra delay in the two-way travel time from the radar to the ground and back (Manzoni et al. 2020). By exploiting SAR images, it is possible to generate delay maps called Atmospheric Phase Screens (APS) which can be used for numerous applications, including weather forecasting, climate modeling, and aviation safety (Mateus et al. 2016; Meroni et al. 2020). In recent years, there have been significant advances in SAR-based retrieval of atmospheric phase screens, including developing new algorithms and incorporating additional information from other sensors. In this paper, we will describe the processing scheme used to estimate APS using a stack, and detail a calibration procedure based on a Global Navigation Satellite System (GNSS) network on the ground needed to remove orbital artifacts from the estimated tropospheric maps.

As for the ionosphere, the EM senses the space-varying Total Electron Content (TEC) (Meyer et al. 2006). The amount of electrons changes with latitude, season, time of day, and stochastic events. The value of the refractive index is inversely dependent on the frequency, causing a dispersive effect on the radio signal. The measured delay is always positive, but the phase is negative, which makes it distinguishable from other phase contributions, for example, by the split spectrum method (Gomba et al. 2015). While the influence of the ionosphere is particularly strong at lower frequencies (L- or P- bands), it is still present also at C-Band and can eventually prevent accurate estimation of deformations or tropospheric water vapor maps (Belcher and Rogers 2009). Two different components can be distinguished in the TEC distribution: large-scale effects and local perturbations; however, the latter is primarily an equatorial and high-latitude phenomenon and will not be treated in the following analysis. In this paper, we will describe ionospheric effects on SAR images and their mitigation by estimating the ionospheric component, which can then be removed from SAR interferograms to improve

derived unbiased products. The novelty of the proposed method lies in the fact that the split-spectrum estimation is performed directly from coregistered images, without the need to perform any prior processing. This fact makes the technique suitable to be an add-on to existing processing chains. Furthermore, the exploitation of an optimal stack-based phase estimator is an improvement with respect to the standard workflow based on a single interferometric pair.

The paper is organized as follows: in Section 2, the procedure for APS estimation is detailed, as well as the SAR-GNSS cross-calibration. In the same section, results and validation are provided. In Section 3, we present the processing workflow for the estimation of the ionospheric component along with results obtained with Sentinel-1 data and with a qualitative validation of the technique. In the last section, conclusions are drawn.

## 2. Atmospheric phase screen estimation with GNSS cross-calibration

The effect of the atmosphere has always been seen as a disturbance in InSAR processing, posing challenges to accurate data interpretation. The variations in pressure, temperature, and humidity along the path traveled by the electromagnetic (EM) wave from the satellite to the ground create a non-unitary refractive index. As a consequence, the phase of the SAR image is disturbed, making it challenging to obtain precise measurements of deformation rates or generate DEM, which are vital outcomes of InSAR.

However, in recent years, a new field has emerged in the scientific community known as InSAR Meteorology (Mateus et al. 2016). This discipline recognizes that the excessive path delay caused by the atmosphere is intrinsically linked to the refractive index, which is closely associated with the water vapor content present in the atmosphere. This realization suggests that it is possible to leverage InSAR data to assimilate information into Numerical Weather Prediction Models (NWPM) (Pichelli et al. 2014). What was once perceived as a disturbance is now considered a signal of interest.

Despite this paradigm shift, several challenges persist in effectively estimating the Atmospheric Phase Screen (APS) over both Permanent Scatterers (PS) and Distributed Scatterers (DS). Accurately calibrating the atmospheric phase screen is essential to eliminate orbital inaccuracies that have the potential to corrupt the ingestion product if left unaddressed. Therefore, the scientific community is actively exploring methods and techniques to reliably estimate the APS and develop robust calibration procedures to compensate for these orbital effects. By overcoming these hurdles, researchers aim to enhance the quality and accuracy of

InSAR data, enabling its broader application in meteorology and weather prediction models.

This part of the paper is dedicated to describing the algorithm used to extract APS starting from a stack of SAR images. The pre-processing procedure will be detailed, and the optimal phase estimator will be described. The same is valid for the orbit calibration procedure. At the end of the chapter, the results provided by the technique are shown and discussed.

## 2.1. Processing chain

The entire processing chain is explained in detail in this section, starting from the pre-processing procedures to the final calibration with GNSS. Figure 1 depicts a comprehensive block diagram. Notice that both the tropospheric and ionospheric phase estimation workflows are represented in this scheme. The pre-processing procedure, common to both processing, is depicted in the orange box, while the processing chain to extract tropospheric maps is shown in the green box. Finally, the ionospheric processing is represented in the blue box.

### 2.1.1. Pre-processing

The input data is a set of Sentinel-1 (C-Band) SAR images acquired over the same scene with a temporal baseline of 6–12 days. The first step in the pre-processing chain is to focus all the raw data to obtain Single Look Complex (SLC) radar images of the scene under study. All the SLCs must be registered to the same reference one in a process called *coregistration*. The second step compensates for each image's reference and topographic phases. The interferometric phase, in fact, contains deformation, atmospheric effects, topographic phase, and noise. If the study aims to estimate the atmospheric component, all the others must be compensated or mitigated. The

topographic component can be removed using a prior, which, in this case, is a DEM of the area of interest. All the steps up to this point are carried out using the free and open-source software SNAP, distributed by ESA. The DEM used for topographic phase compensation is the GLO-30 Copernicus DEM. The SAR stack is now ready to be processed either by the ionospheric or the tropospheric estimation processing chain. In the workflow dedicated to the troposphere, in particular, for the orbit correction procedure, it is needed to have some ancillary information about the troposphere provided by a network of GNSS stations installed on the ground. The raw data acquired by the stations must be processed to extract atmospheric products, particularly the Zenith Total Delay (ZTD) in the station's location. The free and open-source application, goGPS (Realini and Reguzzoni 2013), was used to process the raw GNSS data. It is out of the scope of this paper to go into details about the estimation of the atmospheric signal using GNSS data.

### 2.1.2. Phase linking

This section describes the core of the entire tropospheric estimation processing chain. The algorithm used to estimate the interferometric phases is the well-known Phase Linking (Monti-Guarnieri and Tebaldini 2008). This algorithm provides a high-quality estimate of the InSAR phase in the presence of both PS and DS. As demonstrated in (Manzoni, Monti-Guarnieri, and Molinari 2021), this estimator can perform better than classical InSAR phase estimators. One example of such an InSAR phase estimator is the so-called DInSAR estimator, which evaluates the interferometric phase at different temporal baselines. Given the estimated temporal covariance (or coherence) matrix  $\hat{C}$  the  $i^{\text{th}}$  interferometric phase can be estimated as:

$$\psi_i = \hat{C}(1, i + 1) \quad (1)$$

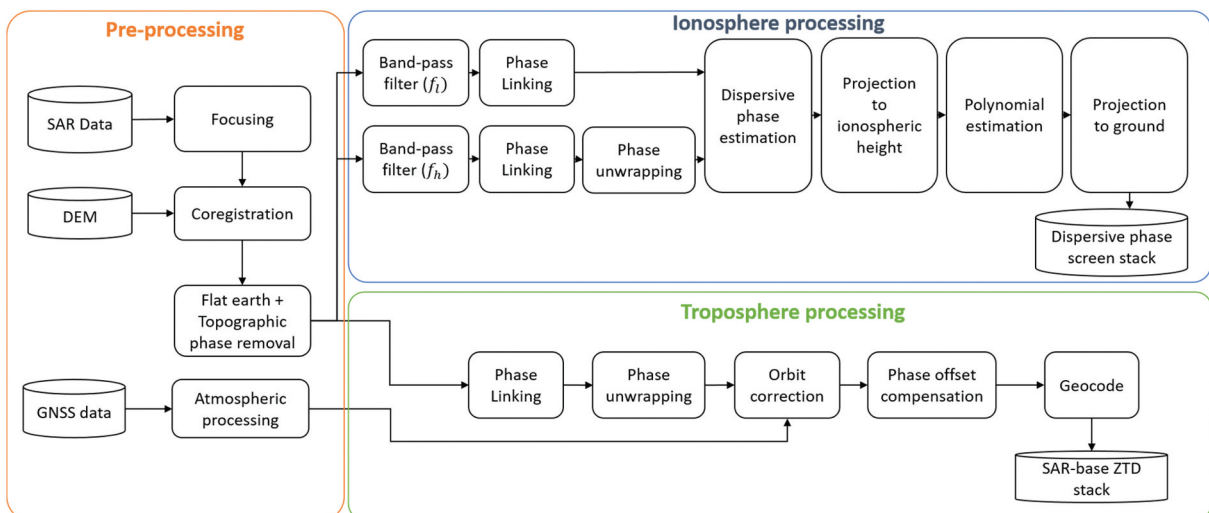


Figure 1. Block diagram of the proposed procedure.

The first argument of the parenthesis indicates the row of the covariance matrix, while the second one is the column. The evident problem for this phase estimator is the temporal decorrelation. The more we increase the temporal baseline, the more temporal decorrelation plays an important role in corrupting the InSAR phase. This consideration suggests that there are better choices than this specific estimator in areas with severe decorrelation. Another possible estimator is the so-called auto-regressive of the first order, also called AR(1). The name derives from the fact that it is the optimal estimator if the decorrelating process acts like an auto-regressive process of the first order. In this case, the  $i^{\text{th}}$  interferometric phase can be defined as:

$$\psi_i = \angle \prod_{k=1}^i \widehat{\mathbf{C}}(k, k+1) \quad (2)$$

where  $\widehat{\mathbf{C}}(k, k+1)$  indicates the sample at row  $k$  and column  $k+1$  of the estimated coherence matrix. The reasoning behind this estimator is that it uses just the images at a short temporal baseline avoiding in this way to deal with poorly coherent interferograms. In this case, the disadvantage is that the phases are integrated; thus, the noise is accumulated. The problem is particularly relevant with long time series and when the images at short temporal baseline show poor coherence due to severe temporal decorrelation. The solution proposed by Phase Linking is to exploit the whole covariance matrix, or, in other words, all the  $N(N-1)/2$  interferograms in it. Phase Linking tries to find the  $N-1$  phases that better fit all the phases in the covariance matrix. The result is a robust estimator able to cope with temporal decorrelation that reaches optimal performances in the presence of stable PSs and decorrelating DSs. The Phase Linking is a generic phase estimator not tuned for a specific application such as APS estimation. We highlight that the estimation window size must be carefully adjusted to obtain a reliable estimate of the atmospheric phase screen. The interferometric phase's quality is tightly related to the number of independent looks used to estimate the coherence matrix. For an interferometric couple, the variance of the estimate of the interferometric phase can be calculated in closed form as (Bamler and Hartl 1998):

$$\sigma_{\psi}^2 = \frac{1 - \gamma^2}{2L\gamma^2} \quad (3)$$

where  $L$  is the number of independent looks used, and  $\gamma$  is the coherence of the scene. If we have a scene with poor coherence, we can still extract a reliable estimate of the interferometric phase by exploiting many independent looks. If we assume an exponential decay of the coherence with a temporal constant of 6 days (i.e. the

target will lose 64% of its coherence in 6 days), 10 images in the stack separated by a temporal baseline of 6 days and a required standard deviation of 1 mm we obtain a minimum of 600 looks. This number of looks is achievable by taking roughly 3000 pixels in a Sentinel-1 image spanning an area of  $375 \times 375 \text{ m}^2$ . This dimension is also the resolution of the estimated APS, which is at least one order of magnitude finer than any high-resolution NWPM. This proves the capability of SAR maps to achieve the requirements in terms of spatial resolution for the ingestion of products into NWPM. Once the phase has been estimated, it is still wrapped (i.e. known just modulo  $2\pi$ ). A reliable and efficient phase unwrapping procedure must be implemented to unwrap large-scale interferograms without generating artifacts.

### 2.1.3. Unwrapping

Unwrapping is a well-known problem that several works have tackled in literature (Murdaca, Rucci, and Prati 2022; Zebker and Lu 1998). We will not investigate the issue since it is not the paper's core. The only remark that must be made is that, in some cases, the phase unwrapping procedure may generate errors called *phase islands*. In particular, when an area is surrounded by a low coherence "belt" in the interferogram, the same spot in the unwrapped interferogram may appear with a  $2\pi$  shift with respect to the rest of the image. In real scenarios, these errors usually occur when regions of poor coherence, such as rivers or forests, delimit an area of the scene. One possible solution is to use a spatial smoothing filter that will reduce the variance of the interferometric phase allowing for a correct unwrapping. For this work, we implemented a 2D unwrapping software from the literature (Zebker and Lu 1998).

### 2.1.4. GNSS cross-calibration

The flat earth and topographic phase compensation procedure described in the pre-processing section of this chapter require precise knowledge of the satellite's orbit during acquisition. If such information is available with insufficient accuracy, some phase artifacts will arise in the interferometric phase. In particular, some phase trends will appear in the interferograms, preventing the correct estimation of the APS. The effect of a residual orbit error is usually neglected if the area of interest is tiny or if Orbit State Vectors (OSVs) are known to be very precise. On the other hand, these trends can be removed by a simple fitting and removal of a plane from the interferogram map. This procedure cannot be applied when the estimate of interest is the APS. In fact, the APS itself can be modeled similarly, and the result would be to invalidate the atmospheric map generated: part of the signal of interest will be considered an orbital error and

removed. The solution proposed here is to use a network of GNSS stations installed on the ground.

Each station provides an estimate of the ZTD at the time instant of each SAR acquisition in the stack. It is also worth highlighting that the accuracy of the residual orbit estimation is tightly related to the position of the GNSS stations in the scene, as analyzed in (Manzoni 2022). In particular, it is desirable to have a sufficient number of stations well-spread in the scene, both in ground range and azimuth, in order for the problem to be well-conditioned. The procedure can be described as follows (Manzoni, Monti-Guarnieri, and Molinari 2021):

- Each ZTD estimate of each GNSS station is differentiated in time with respect to the same date of the SAR reference image. In this way, we obtain the GNSS-derived differential ZTD (dZTD).
- Each dZTD is projected in the slant range direction of the SAR by knowing the look angle of the SAR sensor. This angle can be computed by knowing the satellite's orbit and the GNSS station's position. After the projection, we end up with a set of GNSS-derived APS.
- All the derived SAR maps are evaluated (interpolated) over the positions of each GNSS station. We now have a set of SAR-derived APS plus orbital error and a set of GNSS-derived APS.
- From each SAR estimate, the GNSS-derived APS are removed. If the orbital error is zero, the residual should be just noise and, eventually, the deformation of the scene. On the other hand, if there is an orbital error, the residual is the measurement that will be used to estimate the parameters of the orbital error itself (the normal baseline error and the derivative of the line of sight baseline with time).
- A linear system of equations is solved in robust  $L1$  norm to derive the estimate of the orbital error's parameters.
- A set of Orbital Phase Screens (OPS) are computed and compensated from all the interferograms.

This procedure results in a set of calibrated APS in which the trend due to orbital inaccuracies has been removed. In the following sections, some results using the Sentinel-1 constellation are presented.

### 2.1.5. Phase offset compensation

It is well known that SAR interferometry is also differential in space. Thus, it makes sense only to evaluate a phase *difference* between two points in space. In other words, SAR interferograms are missing a constant to be absolute. Such a constant must be injected with an external measurement, such as GNSS data. After the orbital correction, the only difference (apart from noise) that should be present between the SAR-derived APS and the GNSS-derived APS is a constant. Its estimation is then trivial by taking once again the difference between the two estimates (GNSS and SAR) and averaging over all the available measurements.

## 2.2. Results

This section presents the result obtained by exploiting the procedure just explained. We used a set of SAR images from the European Space Agency (ESA) Copernicus Sentinel-1 mission for all the experiments. The first case study involves a large region in South Africa. We processed six Sentinel-1 frames leading to an APS map of roughly  $170 \times 800$  km<sup>2</sup>. The area also shows significant topography and is generally poorly coherent, even with a short temporal baseline. The average 12-day coherence of the scene is lower than 0.4. Nevertheless, it is possible to estimate reliable phases from the SAR images using a large estimation window (in the order of  $375 \times 375$  m<sup>2</sup> on the ground). In Table 1 a summary of the SLC used for the South African case study is presented. The relative orbit used is the number 43 in ascending configuration.

In Figure 2 the frame and the available GNSS stations are depicted. Next to each frame contour, the frame number is highlighted. In Figure 3(a), an example of estimated APS is depicted. The holes in the picture are areas where the phase is unreliable and therefore discarded. As a rule of thumb, we discard all the phase measurements with coherence lower than 0.2. These spots are, for example, waterbodies or regions with very poor interferometric coherence. To statistically characterize the APS maps, the spatial variograms have been computed. The wet delay has a magnitude much smaller than the hydrostatic one (typically less than 10% of the total slant delay), but its fluctuations are more significant both in time and space. In Figure 3(b) we selected a random region in

**Table 1.** Platform, date, and temporal baselines for the six acquisitions in the South African case study.

Platform	Data	Step-one temporal baseling	Total temporal baseline
S1A	01/02/2018	–	–
S1A	13/02/2018	12 days	12 days
S1A	25/02/2018	12 days	24 days
S1A	09/03/2018	12 days	36 days
S1A	21/03/2018	12 days	48 days
S1A	02/04/2018	12 days	60 days

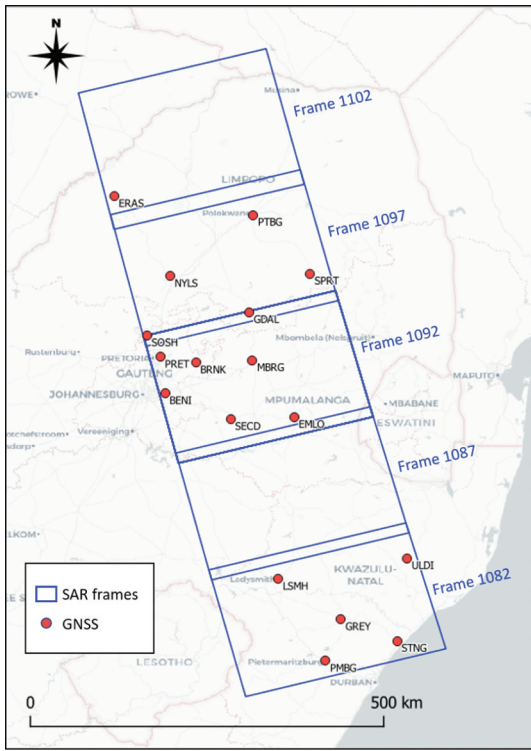


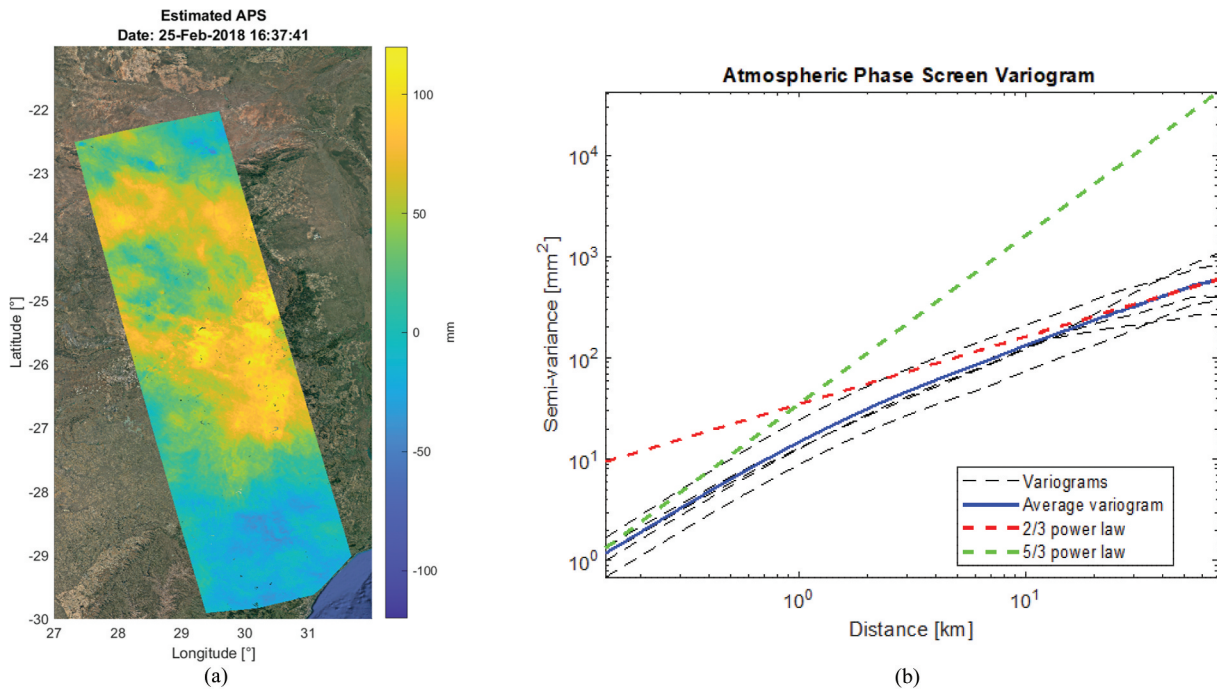
**Figure 2.** Frame numbers and GNSS stations in the South Africa case study.

all the estimated APS and computed the spatial variograms. All the variograms for the five images are depicted in black dashed lines. The average variogram is represented in blue, while in red and green, the 2/3 power law and 5/3 power law are, respectively, depicted. A transition region between the two models is predicted at around 1.5 km (intersection between

red and green lines) (Hanssen 2001; Tatarski 2016). At longer wavelengths, the tropospheric signal starts to be less turbulent and more correlated in space, leading to a smaller slope of the red curve. From the figure, it is evident that the data follow the theoretical model both for each image and on average. The scarce number of GNSS stations in this region prevents a validation with another dataset. All the available stations were used for the orbital calibration and, therefore, cannot be used for a fair comparison between SAR and GNSS.

The second case study was performed in Sweden. The information about the acquisition dates is represented in Table 2. The relative Sentinel-1 orbit is the number 168. As in the previous case study, the scene is very unstable, showing poor coherence as depicted in Figure 4. Notice that the image is in radar coordinates this time and not in the geographic ones as in Figure 3(a).

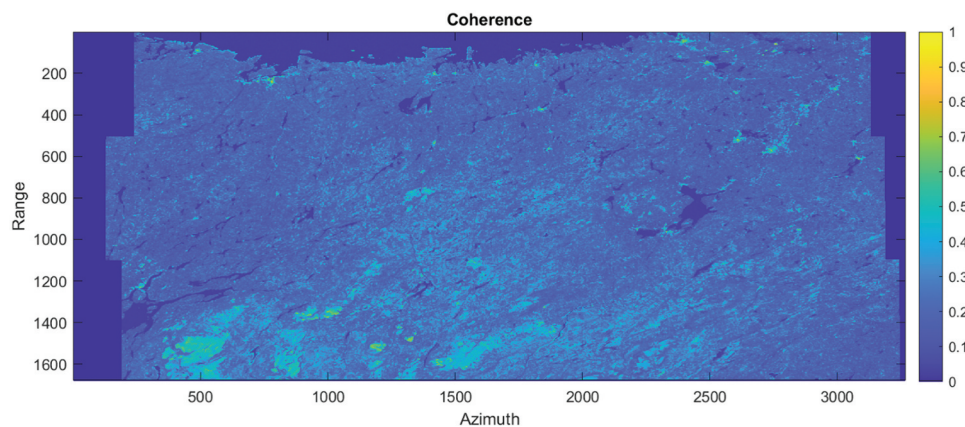
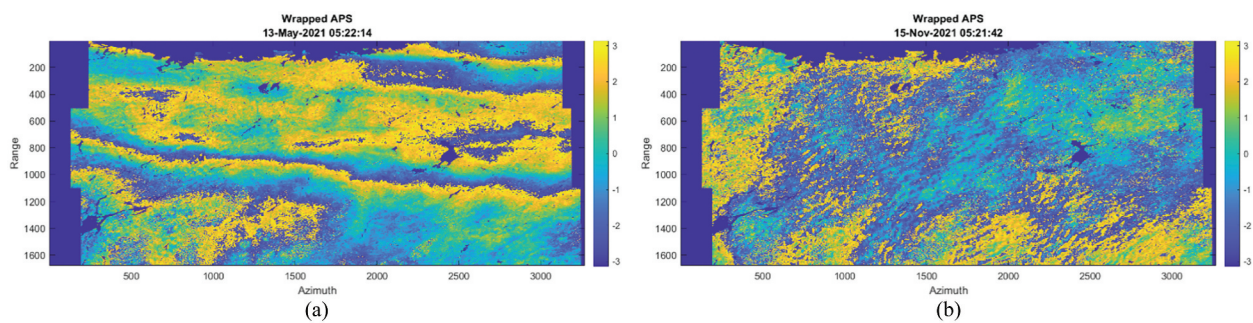
Unlike the first case study, in this one, we processed 33 images spanning a total temporal extent of 6 months. Thanks to its intrinsic robustness, the Phase Linking algorithm can still provide reliable phase maps even with these long temporal baselines. A wrapped APS is depicted in Figure 5(a). In this image, an equivalent temporal baseline of 6 days was used. The phase profile is smooth, as expected, and it can be easily unwrapped. In Figure 5(b), on the other hand, we show the last APS of the stack with a temporal baseline of roughly 6 months with respect to the first image (the reference image was acquired the 1st of May 2021). While this image shows a higher spatial variability than the former example, it is still very



**Figure 3.** (a) An example of an estimated APS. The size of the map is  $170 \times 800 \text{ km}^2$ . (b) Variograms of the estimated APS maps. They follow the theoretical model.

**Table 2.** Platform, date, and temporal baselines for the six acquisitions in the Sweden case study.

Platform	Data	Step-one temporal baseling	Total temporal baseline
S1A	01/05/2021	–	–
S1A	13/05/2021	6 days	12 days
S1A	25/05/2021	6 days	24 days
S1A	31/05/2021	6 days	36 days
S1B	06/06/2021	6 days	48 days
S1A	12/06/2021	6 days	60 days
S1B	18/06/2021	6 days	72 days
S1A	24/06/2021	6 days	78 days
S1B	30/06/2021	6 days	84 days
S1A	06/07/2021	6 days	90 days
S1B	12/07/2021	6 days	96 days
S1A	18/07/2021	6 days	102 days
S1B	24/07/2021	6 days	108 days
S1A	30/07/2021	6 days	114 days
S1B	05/08/2021	6 days	120 days
S1A	11/08/2021	6 days	126 days
S1B	17/08/2021	6 days	132 days
S1A	23/08/2021	6 days	138 days
S1B	29/08/2021	6 days	144 days
S1A	04/09/2021	6 days	150 days
S1B	10/09/2021	6 days	156 days
S1A	16/09/2021	6 days	162 days
S1B	22/09/2021	6 days	178 days
S1A	28/09/2021	6 days	184 days
S1B	04/10/2021	6 days	190 days
S1A	10/10/2021	6 days	196 days
S1B	16/10/2021	6 days	202 days
S1B	28/10/2021	6 days	214 days
S1A	03/11/2021	6 days	220 days
S1B	09/11/2021	6 days	226 days
S1A	15/11/2021	6 days	232 days
S1B	21/11/2021	6 days	238 days

**Figure 4.** Coherence map of the area of interest in Sweden. The image is radar coordinates (range/azimuth).**Figure 5.** (a) Wrapped APS map with a temporal baseline of 6 days. (b) Wrapped APS map with a temporal baseline of 6 months. The color scale is in radians.



smooth with low variance. This allows for an easy and reliable phase unwrapping. Finally, proper validation is needed to prove that the signal we are retrieving is exactly the atmospheric one. In the first case study, we used a validation with a theoretical model since there were a small number of GNSS stations on the ground, and they were all used for orbital correction. In this case study, however, more than 100 GNSS stations were present in the field of view, allowing for proper technique validation. We have selected 30 of GNSS in a random fashion. The 30/70 ratio was used in order to have a reliable estimate of the orbital parameters, while, at the same time, having a reliable validation of the procedure. In [Figure 6](#), a scatter plot is depicted for all the dates in the stack. On one hand, we have the SAR-derived APS estimated by the proposed algorithm; on the other, we have the GNSS-derived APS. Notice that the latter is an independent set of GNSS stations that do not coincide with the one used for the orbital calibration. The picture shows a very high agreement between the two datasets, with an average correlation coefficient of 0.99 and a standard deviation of 8.49 mm. As a last notice, we highlight that the GNSS raw data was processed in such a way as to extract purely the tropospheric delay and not the ionospheric one. We proved in this way the capability of the proposed algorithm to extract most of the troposphere dynamics.

### 3. Mitigation of ionospheric phase screen in SAR images for atmosphere analysis

The spatial statistics of the added phase screen due to a slow varying ionosphere is very similar to the APS; thus, it cannot be distinguished by standard filtering methods. The split spectrum method (Rosen, Hensley, and Chen 2010) exploits the dispersive nature of the ionosphere. It aims to separate it from the non-dispersive effects (atmosphere, topography, movement, etc.) by observing the phase at different frequencies. Successful implementation of the technique on S1 data was demonstrated in (Gomba, González, and De Zan 2016), accommodating the peculiarities of the Terrain Observation with Progressive Scans SAR (TOPSAR) acquisition scheme.

This section constructs a processing chain that is adapted to the requirements of atmosphere processing. First, we can assume the scene to be relatively stable over time, which relaxes the need for very fine data-driven coregistration. As will be demonstrated in [Section 3.1.2](#), this assumption significantly simplifies the implementation. Second, a stack of images is usually needed for meaningful atmospheric interpretation. Thus, the ionospheric phase should be removed from all data instances with respect to a common reference. We use the Phase Linking algorithm (Monti-Guarnieri and Tebaldini 2008) to obtain a temporal series and reduce the noise.

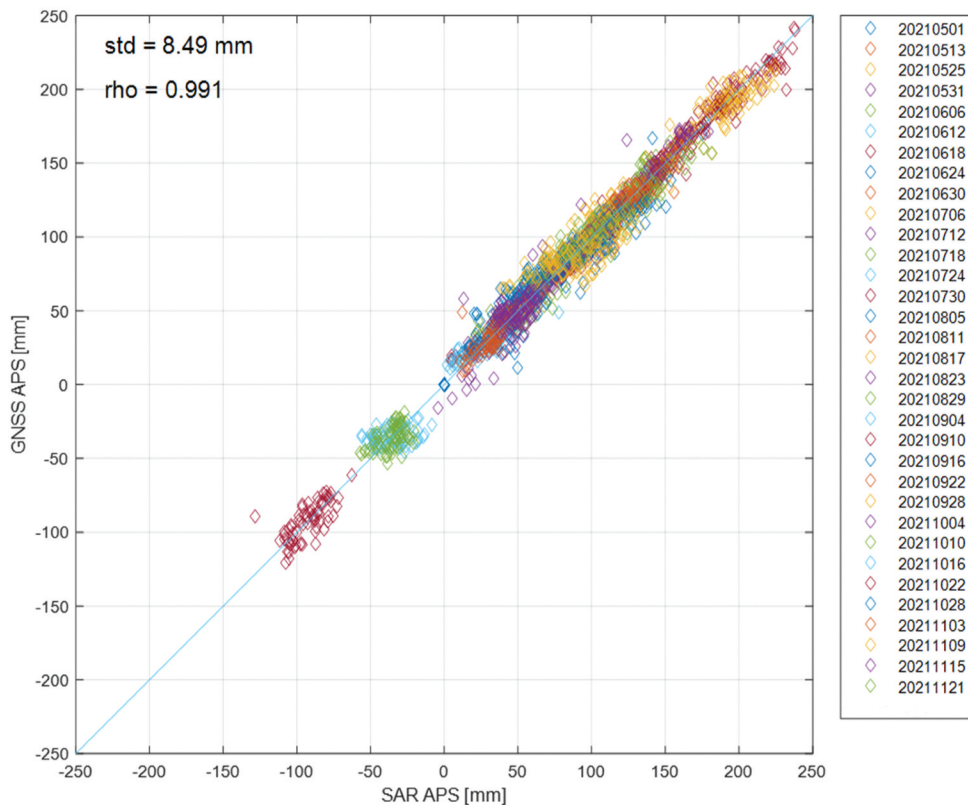


**Figure 6.** Scatterplot of the estimated (SAR) APS with an independent set of GNSS-derived APS.

### 3.1. Processing chain for stack-based ionospheric phase estimation

The overall processing flow for estimating the ionospheric phase screen is shown in Figure 1. First, the same regular pre-processing routines already described in Section 2.2.1 should be performed on all images, including focusing, coregistration, and phase compensation.

The TOPSAR acquisition mode acquires the data in bursts by cyclically switching the antenna beam (Grandin 2015). The sensing technique implies that the ionosphere is not being sampled continuously, and phase jumps between bursts may be expected. Theoretically, the shifts may be measured and corrected by other methods, such as the Enhanced Spectral Diversity (ESD) or cross correlation. However, these techniques cannot recover the proper ionospheric phase screens and compensate the interferogram (Gomba, González, and De Zan 2016). Thus, we apply the split spectrum technique which can provide an accurate estimate of the phase.

The multi-temporal ionosphere estimation module extracts sub-bands in a burst-by-burst fashion, and Phase Linking is applied to the sub-bands of all images to reduce noise. The output is a series of  $N - 1$  phase maps. The unwrapping of at least one sub-bands is required to overcome the  $2\pi$  ambiguity. At this point, the result is still rather noisy because of the significant amplification of the phase difference. Thus, we estimate a polynomial from the raw dispersive phase. The regression is done with the data projected to the height of the ionospheric level (assumed to be constant at 350 km), and the result is projected back to earth. The block scheme's outputs are phase products that can compensate the ionospheric effect in the interferometric stack.

#### 3.1.1. Split-spectrum

The group delay and phase advance of an electromagnetic signal passing through the ionosphere is a function of the frequency:

$$\tau_{group}^i = -\tau_{phase}^i = \frac{2K_0 STEC}{cf^2} \quad (4)$$

where  $K_0 = 40.28\text{m}^3\text{s}^{-2}$ , while STEC is the Slant range Total Electron Content. The frequency dependence allows us to measure  $\tau_{phase}^i$  by extracting two non-overlapping frequency sub-bands. An interferometric approach is required (i.e. processing the complex conjugate of two images) such that the phase contributions related to the target's spectrum are eliminated. The ionosphere can then be estimated by (Gomba, González, and De Zan 2016):

$$\Delta\hat{\phi}_{iono} = \frac{f_L f_H^2}{f_0(f_H^2 - f_L^2)} \left( \Delta\hat{\phi}_L - \frac{f_L}{f_H} \Delta\hat{\phi}_H \right) \quad (5)$$

where  $f_0$  is the frequency of the carrier.  $\Delta\hat{\phi}_L$ ,  $\Delta\hat{\phi}_H$  are the interferometric phases of the two sub-bands, generated around the frequencies  $f_L$  and  $f_H$ , respectively.

Note that the expression in brackets in Equation (5) is not expected to wrap. Thus, in the proposed implementation of the split spectrum method, it is sufficient to unwrap only one band. An explicit description of the performed operation is given by:

$$\Delta\hat{\phi}_{iono} = \frac{f_L f_H^2}{f_0(f_H^2 - f_L^2)} \angle \left[ \exp(\Delta\hat{\phi}_L) \exp\left(-j\frac{f_L}{f_H} \Delta\hat{\phi}_H^{\text{unwrap}}\right) \right] \quad (6)$$

#### 3.1.2. Effect of coregistration

Current state-of-the-art implementations of the split-spectrum method generate two sub-bands from each focused data and coregistering them afterward (Liang et al. 2019). The method implies that resampling should be repeated for the original data and for the two bands. For many applications, it is beneficial to start directly from the coregistered data, as illustrated in Figure 1. In this manner, one gains in terms of computational power and storage. The suggested approach uses the precise knowledge of the S1 orbits to coregister and compensate the phase. The residual can then be explored by the split spectrum algorithm to estimate the ionospheric phase screen. This section demonstrates the equivalence of the two strategies, by theoretically analyzing the spectrum of the coregistered data.

The spectrum of an interferometric SAR pair (after demodulation) can be expressed as:

$$M(f) = A(f) \quad (7)$$

$$S(f) = A(f) e^{(-j2\pi f_0 \tau(f))} e^{(-j2\pi f \tau(f))} \quad (8)$$

being  $M(f)$  and  $S(f)$  the master and slave signals, respectively.  $A(f)$  is the spectra of the low-pass reflectivity function of the target, and  $\tau$  is the time delay between the two acquisitions. The first exponential is the interferometric phase, and the second is the frequency ramp due to misregistration. The uncompensated delay between master and slave  $\tau$  is due to all the residual effects:

$$\tau(f) = \tau_{geo} + \tau_{APS} + \tau_{phase}^i(f) \quad (9)$$

where  $\tau_{geo}$  is the geometrical component due to flat earth and topography.  $\tau_{APS}$  and  $\tau_{phase}^i(f)$  are the delays caused by the atmosphere and ionosphere, respectively. Other non-dispersive effects are omitted here for simplicity.

After coregistration and compensation of the geometrical phase, the slave from Equation (8) becomes:

$$S_C(f) = A(f)e^{-j2\pi(f_0+f)(\tau_{APS}-\tau_{phase}^i(f_0+f))} \quad (10)$$

At this point, the range spectrum is divided into two sub-bands by applying band-pass filters centered at  $f_i$  for  $i = 1, 2$ :

$$S_{ci}(f) = S_c(f)\text{rect}\left(\frac{f-f_i}{B_s}\right) \quad (11)$$

where  $B_s$  is the bandwidth of the filter. The bands are further demodulated by  $f_i$  to obtain two baseband signals:

$$S_{ci0}(f)|_{f=0} = A(f_i)e^{-j2\pi(f_0+f_i)(\tau_{nd}-\tau_{phase}^i(f_0+f_i))} \quad (12)$$

The phase in Equation (12) is equal to the one we would get applying the coregistration after band extraction.

### 3.2. Stack processing

A time series of interferometric SAR information is of interest for many use cases. For example, the usage of a SAR stack to estimate the atmospheric phase screen in Section 2.2. Thus, also the ionospheric screen should be evaluated for multiple images w.r.t. a common reference. The joint estimation of the dispersive phase for a stack of SAR images was explored in (Fattahi, Simons, and Agram 2017), using a set of linear equations. In the current method, we use the phase-linking approach (see Section 2.1.2) on each sub-band. In doing so, we exploit all possible interferometric combinations to reduce the variance and obtain  $N - 1$  phase screens.

### 3.3. Study area and results

The proposed scheme was tested on the border between Chile and Argentina, a site that was shown

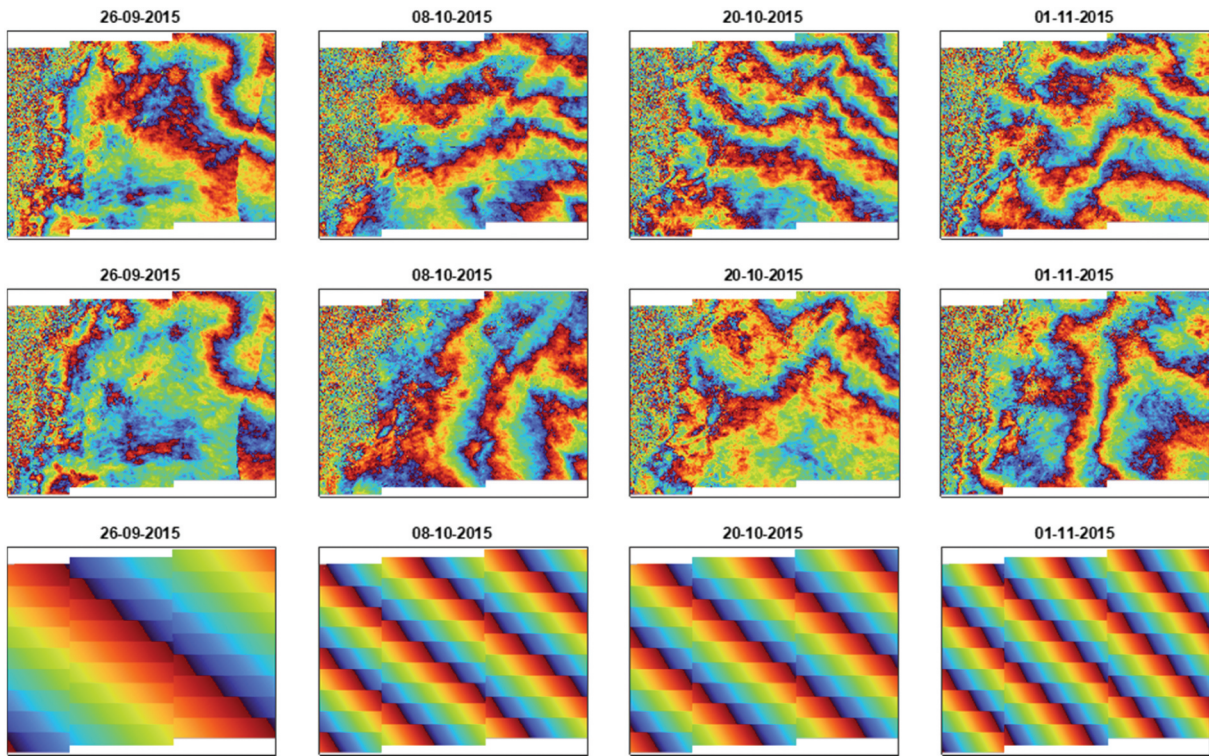
to be affected by a significant ionospheric gradient during the S1 acquisition in the fall of 2015 (Gomba 2018). It was not possible to use the same scenarios used in Section 2.2 due to the absence of a strong ionospheric signal in those regions. Figure 7 shows the footprint of the relevant S1 frame. A major part of the scene is characterized by flat terrain with rocky and sandy soils and an arid climate, which results in an overall high spatial and temporal coherence. Five images were used over a period of 2 months.

The estimation and compensation of the ionospheric phase screen were performed following the scheme described in Figure 1. Note that the interferometric processing is able to recover  $N - 1$  phases (using one reference image), so only the relative ionosphere can be computed using this technique. A proper validation was not possible in this case due to a lack of independent data at sufficient resolution able to provide a serious comparison for SAR-derived ionospheric data. However, a qualitative comparison between the interferograms before and after the compensation of ionospheric fringes is still possible. These interferograms are shown in Figure 8. The first row of images shows the original differential phase, where significant ramps are caused by the ionosphere. The second row shows the stack after the removal of the trends estimated by the split spectrum. Finally, the third row shows the ionospheric phase screen. First-order polynomials were used in this study because of the observed dispersive phase.

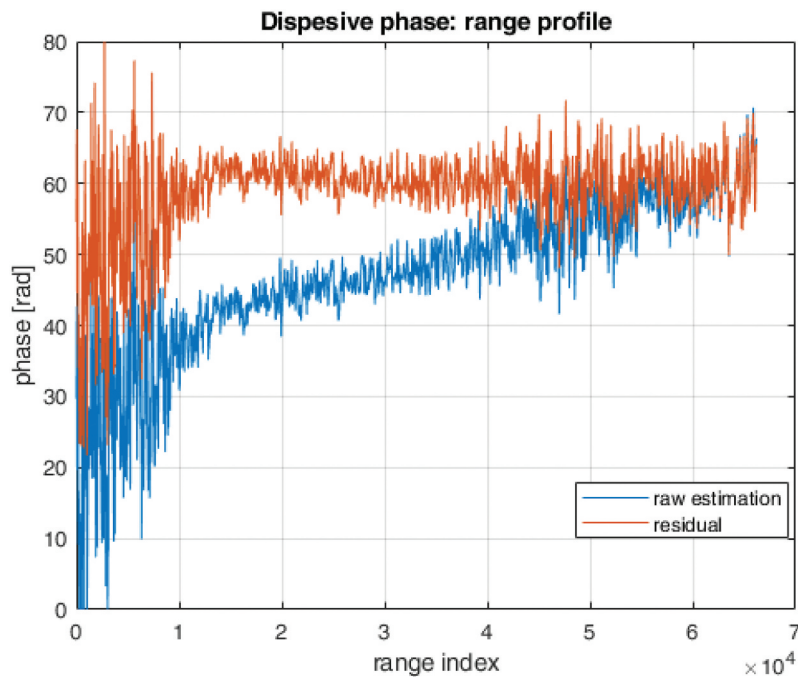
Strong phase ramps are noticed in the last three interferograms, accompanied by noticeable discontinuities between the bursts. The phase jumps remain after coregistration since no data-driven resampling was performed. However, they are well predicted by the estimated ionospheric phase screens taking into account the gapped scanning of the ionosphere by the TOPSAR acquisition mode. As a result, the corrected interferograms are continuous.



Figure 7. Region of interest used in the study. Basemap by Google.



**Figure 8.** Ionosphere compensation results. Top: original interferograms (master date: 02-09-2015) with visible phase jumps between burst due to the presence of ionospheric gradient. Middle: compensated interferograms, the phase jumps were mitigated. Bottom: estimated phase screen. Values are in the range of  $[-\pi, \pi]$ .



**Figure 9.** Dispersive phase for the 01-11-2015 interferogram, averaged along the azimuth axis. A clear linear trend is observed in the raw estimate (blue). After removing the estimated phase screen the residual is mainly flat (orange).

The dispersive phase in the selected case-study showed a major linear trend, as can be appreciated from the range profile in Figure 9. Thus, a first-order polynomial was utilized for the estimation. Higher orders may be considered for other data-sets.

Phase linking was introduced to decrease the noise in the data. An improvement in STD w.r.t. the single-baseline approach can be observed, especially for the last images in the time-series, since decorrelation becomes more significant. The local standard

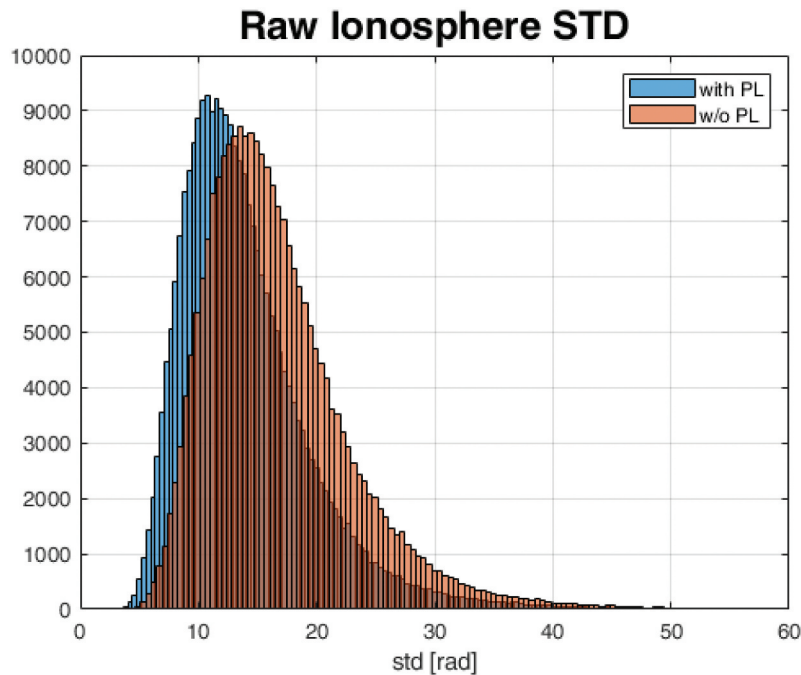


**Figure 10.** Effect of phase linking on the standard deviation of the raw ionospheric phase screen estimate. The measure was taken for the last image in the stack, where the noise level due to decorrelation is higher.

deviation (STD) of the raw ionosphere estimate is shown by a histogram in Figure 10.

#### 4. Conclusions

This paper discusses two techniques in SAR atmospheric sensing. The first topic is the estimation of atmospheric phase delay maps from a stack of SAR images. The proposed technique exploits the well-known Phase Linking algorithm in combination with a novel calibration scheme used to remove orbital errors. This calibration scheme is data-driven and uses a network of GNSS stations on the ground to estimate and remove a low-frequency phase trend that arises when the orbital knowledge of the satellite is not accurate enough. Combining the optimal estimator and the calibration procedure allows us to estimate the tropospheric component in the interferometric phase accurately. We validated the method's effectiveness using statistical comparisons with the theoretical models and an external set of GNSS measurements. The correlation between our estimate and the independent GNSS measure is close to one, proving the method's effectiveness.

In the second part of the paper, we have demonstrated a fast and effective implementation of the split-spectrum algorithm applied to Sentinel-1 data. Also, in this case, the novelty is that we jointly exploit a set of SAR images, gaining from all the available interferograms to reduce the noise and partially compensate for the lack of data-driven coregistration. In contrast to the state-of-the-art workflows for ionospheric

signal extraction, we start the procedure by coregistering data immediately before sub-band extraction, allowing greater compatibility with standard InSAR processors. Testing was performed using data acquired over Chile, a site where the ionosphere is known to vary rapidly. The compensation showed a significant reduction in phase jumps between bursts and an overall reduction in the number of fringes. Only coregistered data was used during estimation and compensation, making the approach appealing for integration into existing interferometric tools.

#### Disclosure statement

No potential conflict of interest was reported by the author(s).

#### Funding

This paper was prepared to summarize the research conducted during the first 2 years of research at the mid-term stage of the Dragon 5 project 59332 (Geophysical and atmospheric retrieval from SAR data stacks over natural scenarios). The activities are funded by the European Space Agency under contract [4000136890/21/I-NB].

#### Notes on contributors

**Marco Manzoni** was born in Lecco, Italy, in 1994. He received a B.Sc. (2016), M.Sc. (2018), and Ph.D. (2022) in Telecommunication engineering from Politecnico di Milano. His research is focused on signal processing techniques for radar remote sensing, including spaceborne and car-borne Synthetic Aperture Radar signal

processing, water vapor estimation from space-borne interferometric SAR measurements, and change detection. He is currently involved in the interferometric commissioning phase of the new Copernicus Sentinel-1C mission.

**Naomi Petrushevsky** received the M.S. degree (cum laude) in Geoinformatics from Politecnico di Milano, in 2020. Currently, she is pursuing her Telecommunications Ph.D. degree in Politecnico di Milano. Her research activities focus on interferometric processing SAR systems, including MIMO calibration, extraction of ionospheric phase screens, displacement estimation and classification. She is part of the interferometric commissioning phase of the new Copernicus Sentinel-1C mission.

**Chuanjun Wu** received the M.S. degree in Geomatics Engineering and is currently pursuing the Ph.D. degree in Wuhan university. He studied for 2 years as an exchange Ph.D. student at Politecnico di Milano. His research interests are SAR tomography for forest application, including inversion of forest height, underlying topography, and above-ground biomass.

**Stefano Tebaldini** received the M.S. degree in telecommunication engineering and the Ph.D. degree from the Politecnico di Milano, in 2005 and 2009, respectively. Since 2005, he has been with the Digital Signal Processing Research Group, Politecnico di Milano, where he currently holds the position of Associate Professor.

His research activities mostly focus on Earth Observation with Synthetic Aperture Radar (SAR) and Radar design and processing. He is one of the inventors of a new technology patented by T.R.E. for the exploitation of multiple interferograms in the presence of distributed scattering. He teaches courses on signal theory and remote sensing at the Politecnico di Milano. He has been involved as a key scientist in several studies by the European Space Agency (ESA) concerning the tomographic phase of BIOMASS. He was a member of the SAOCOM-CS ESA Expert Group and is currently a member of the BIOMASS MAG at ESA.

**Andrea Virgilio Monti-Guarnieri** received the M.Sc. degree (cum laude in electronic engineering), in 1988. He has been a Full Professor with the Dipartimento di Elettronica, Informazione e Bioingegneria, since 2017. He is the Founder of PoliMi spin-off Aresys (2003), targeting SAR, radar, and geophysics applications. He has an H index (Google) of 33, 5400 citations, received four conference awards, and holds applications for five patents. His current research interests focus on radar-based system design, calibration, MIMO, and geosynchronous SAR. He has been a reviewer of several scientific journals, Guest Editor for MPI Remote Sensing, and a member in scientific-technical committees of international workshops and symposia on Radar and Earth Observation (EO).

**Mingsheng Liao** is a professor in Wuhan University. He has published more than 100 peer-reviewed journal papers and four books focused on synthetic aperture radar interferometry techniques and applications. His research interests include algorithms and application for interferometric synthetic aperture radar, remote sensing image processing and analysis, and the integration and fusion of multisource spatial information.

## ORCID

Marco Manzoni  <http://orcid.org/0000-0002-5525-0491>  
Naomi Petrushevsky  <http://orcid.org/0000-0002-6591-1433>

Chuanjun Wu  <http://orcid.org/0000-0002-3854-8683>  
Stefano Tebaldini  <http://orcid.org/0000-0002-1229-3811>  
Andrea Virgilio Monti-Guarnieri  <http://orcid.org/0000-0003-2142-7807>

Mingsheng Liao  <http://orcid.org/0000-0001-9556-4287>

## References

- Bamler, R., and P. Hartl. 1998. "Synthetic Aperture Radar Interferometry." *Inverse Problems* 14 (4): R1–54. <https://doi.org/10.1088/0266-5611/14/4/001>.
- Belcher, D. P., and N. C. Rogers. 2009. "Theory and Simulation of Ionospheric Effects on Synthetic Aperture Radar." *IET Radar, Sonar & Navigation* 3 (5): 541. <https://doi.org/10.1049/iet-rsn.2008.0205>.
- Fattahi, H., M. Simons, and P. Agram. 2017. "InSAR Time-Series Estimation of the Ionospheric Phase Delay: An Extension of the Split Range-Spectrum Technique." *IEEE Transactions on Geoscience and Remote Sensing* 55 (10): 5984–5996. <https://doi.org/10.1109/TGRS.2017.2718566>.
- Ferretti, A., C. Prati, and F. Rocca. 2000. "Nonlinear Subsidence Rate Estimation Using Permanent Scatterers in Differential SAR Interferometry." *IEEE Transactions on Geoscience and Remote Sensing* 38 (5): 2202–2212. <https://doi.org/10.1109/36.868878>.
- Gomba, G. 2018. "Estimation of Ionosphere-Compensated Azimuth Ground Motion with Sentinel-1." In *EUSAR 2018; 12th European Conference on Synthetic Aperture Radar*, Aachen, Germany. 1–4.
- Gomba, G., F. R. González, and F. De Zan. 2016. "Ionospheric Phase Screen Compensation for the Sentinel-1 TOPS and ALOS-2 ScanSAR Modes." *IEEE Transactions on Geoscience and Remote Sensing* 55 (1): 223–235. <https://doi.org/10.1109/TGRS.2016.2604461>.
- Gomba, G., A. Parizzi, F. De Zan, M. Eineder, and R. Bamler. 2015. "Toward Operational Compensation of Ionospheric Effects in SAR Interferograms: The Split-Spectrum Method." *IEEE Transactions on Geoscience and Remote Sensing* 54 (3): 1446–1461. <https://doi.org/10.1109/TGRS.2015.2481079>.
- Grandin, R. 2015. "Interferometric Processing of SLC Sentinel-1 TOPS Data." In *FRINGE'15: Advances in the Science and Applications of SAR Interferometry and Sentinel-1 InSAR Workshop, Frascati, Italy, 23-27 March 2015*.
- Hanssen, R. F. 2001. *Radar Interferometry: Data Interpretation and Error Analysis*. Vol. 2. Springer Science & Business Media.
- Hensley, S., P. Rosen, and E. Gurrola. 2000. "The SRTM Topographic Mapping Processor." In *IGARSS 2000. IEEE 2000 International Geoscience and Remote Sensing Symposium. Taking the Pulse of the Planet: The Role of Remote Sensing in Managing the Environment. Proceedings (Cat. No.00CH37120)*, 3:1168–1170. Honolulu, HI, USA: IEEE. <https://doi.org/10.1109/IGARSS.2000.858056>.
- Liang, C., P. Agram, M. Simons, and E. J. Fielding. 2019. "Ionospheric Correction of InSAR Time Series Analysis of C-Band Sentinel-1 TOPS Data." *IEEE Transactions on*

- Geoscience and Remote Sensing* 57 (9): 6755–6773. <https://doi.org/10.1109/TGRS.2019.2908494>.
- Manzoni, M. 2022. “Fast and Robust Estimation of Atmospheric Phase Screens Using C-Band Spaceborne SAR and GNSS Calibration.” PhD Thesis, Politecnico Di Milano, Springer International Publishing Cham.
- Manzoni, M., A. V. Monti-Guarnieri, and M. E. Molinari. 2021. “Joint Exploitation of Spaceborne SAR Images and GIS Techniques for Urban Coherent Change Detection.” *Remote Sensing of Environment* 253:112152. <https://doi.org/10.1016/j.rse.2020.112152>.
- Manzoni, M., A. V. Monti-Guarnieri, E. Realini, and G. Venuti. 2020. “Joint Exploitation of SAR and GNSS for Atmospheric Phase Screens Retrieval Aimed at Numerical Weather Prediction Model Ingestion.” *Remote Sensing* 12 (4): 654. <https://doi.org/10.3390/rs12040654>.
- Mateus, P., J. Catalao, G. Nico, and P. Benevides. 2019. “Mapping Precipitable Water Vapor Time Series from Sentinel-1 Interferometric SAR.” *IEEE Transactions on Geoscience & Remote Sensing* 1–7. <https://doi.org/10.1109/TGRS.2019.2946077>.
- Mateus, P., R. Tome, G. Nico, and J. Catalao. 2016. “Three-Dimensional Variational Assimilation of InSAR PWV Using the WRFDA Model.” *IEEE Transactions on Geoscience and Remote Sensing* 54 (12): 7323–7330. <https://doi.org/10.1109/TGRS.2016.2599219>.
- Meroni, A. N., M. Montrasio, G. Venuti, S. Barindelli, A. Mascitelli, M. Manzoni, A. V. Monti-Guarnieri, et al. 2020. “On the Definition of the Strategy to Obtain Absolute InSAR Zenith Total Delay Maps for Meteorological Applications.” *Frontiers in Earth Science* 8 (October): 359. <https://doi.org/10.3389/feart.2020.00359>.
- Meyer, F., R. Bamler, N. Jakowski, and T. Fritz. 2006. “The Potential of Low-Frequency SAR Systems for Mapping Ionospheric TEC Distributions.” *IEEE Geoscience and Remote Sensing Letters* 3 (4): 560–564. <https://doi.org/10.1109/LGRS.2006.882148>.
- Monti-Guarnieri, A. V., and S. Tebaldini. 2008. “On the Exploitation of Target Statistics for SAR Interferometry Applications.” *IEEE Transactions on Geoscience and Remote Sensing* 46 (11): 3436–3443. <https://doi.org/10.1109/TGRS.2008.2001756>.
- Morishita, Y., and R. F. Hanssen. 2014. “Temporal Decorrelation in L-, C-, and X-Band Satellite Radar Interferometry for Pasture on Drained Peat Soils.” *IEEE Transactions on Geoscience and Remote Sensing* 53 (2): 1096–1104. <https://doi.org/10.1109/TGRS.2014.2333814>.
- Murdaca, G., A. Rucci, and C. Prati. 2022. “Deep Learning for InSAR Phase Filtering: An Optimized Framework for Phase Unwrapping.” *Remote Sensing* 14 (19): 4956. <https://doi.org/10.3390/rs14194956>.
- Petrushevsky, N., M. Manzoni, and A. V. Monti-Guarnieri. 2021. “Fast Urban Land Cover Mapping Exploiting Sentinel-1 and Sentinel-2 Data.” *Remote Sensing* 14 (1): 36. <https://doi.org/10.3390/rs14010036>.
- Pichelli, E., R. Ferretti, D. Cimini, G. Panegrossi, D. Perissin, N. Pierdicca, F. Rocca, and B. Rommen. 2014. “InSAR Water Vapor Data Assimilation into Mesoscale Model MM5: Technique and Pilot Study.” *IEEE Journal of Selected Topics in Applied Earth Observations and Remote Sensing* 8 (8): 3859–3875. <https://doi.org/10.1109/JSTARS.2014.2357685>.
- Realini, E., and M. Reguzzoni. 2013. “GoGps: Open Source Software for Enhancing the Accuracy of Low-Cost Receivers by Single-Frequency Relative Kinematic Positioning - IOPscience.” *Measurement Science and Technology* 24 (11): 115110. <https://doi.org/10.1088/0957-0233/24/11/115010>.
- Rosen, P. A., S. Hensley, and C. Chen. 2010. “Measurement and Mitigation of the Ionosphere in L-Band Interferometric SAR Data.” In *2010 IEEE Radar Conference*, 1459–1463. <https://doi.org/10.1109/RADAR.2010.5494385>.
- Soja, M. J., S. Quegan, M. M. D’Alessandro, F. Banda, K. Scipal, S. Tebaldini, and L. M. H. Ulander. 2021. “Mapping Above-Ground Biomass in Tropical Forests with Ground-Cancelled P-Band SAR and Limited Reference Data.” *Remote Sensing of Environment* 253 (February): 112153. <https://doi.org/10.1016/j.rse.2020.112153>.
- Tatarski, V. I. 2016. *Wave Propagation in a Turbulent Medium*. Courier Dover Publications.
- Wright, P. A., S. Quegan, N. S. Wheadon, and C. D. Hall. 2003. “Faraday Rotation Effects on L-Band Spaceborne Sar Data.” *IEEE Transactions on Geoscience and Remote Sensing* 41 (12): 2735–2744. <https://doi.org/10.1109/TGRS.2003.815399>.
- Zebker, H. A., and Y. P. Lu. 1998. “Phase Unwrapping Algorithms for Radar Interferometry: Residue-Cut, Least-Squares, and Synthesis Algorithms.” *Journal of the Optical Society of America A* 15 (3): 586. <https://doi.org/10.1364/JOSAA.15.000586>.